

Supporting Information

Crystal phase engineering and surface reconstruction in Co-Mn phosphides: unraveling the mechanisms of high-performance water oxidation catalysis

Tingting Tang,^a Yanfang Teng,^a Kuoteng Sun,^c Yanhan liu,^a Zhendong Gao,^a Tayirjan Taylor Isimjan,^b Jingya Guo,^{*a}, Jianniao Tian^{*a} and Xiulin Yang^{*a}

^a *Guangxi Key Laboratory of Low Carbon Energy Materials, School of Chemistry and Pharmaceutical Sciences, Guangxi Normal University, Guilin 541004, China*

^b *Saudi Arabia Basic Industries Corporation (SABIC) at King Abdullah University of Science and Technology (KAUST), Thuwal 23955-6900, Saudi Arabia*

^c *Liuzhou Bureau of EHV Transmission Company of China Southern Power Grid Co. Ltd, Liuzhou 545006, China*

E-mail addresses: *xlyang@gxnu.edu.cn* (X. Yang); *jyguo@gxnu.edu.cn* (J. Guo);
birdtjn@sina.com (J. Tian).

1. Experimental sections

Materials characterization

The structural integrity of the samples was characterized using X-ray diffraction (XRD) analysis performed on a Rigaku 13 D/Max 2500 V/PC instrument (Japan). The morphology and microstructure of the samples were characterized using field-emission scanning electron microscopy (SEM, FEI Quanta 200 FEG) and transmission electron microscopy (TEM, JEM-2100F). Raman spectra were obtained using micro-confocal Raman spectroscopy (InVia Qontor, Renishaw) with a 785 nm laser as the excitation source. Electron paramagnetic resonance (EPR) spectra were recorded using a Bruker E500 spectrometer. The specific surface area and pore size distribution of the catalyst were determined using the Brunauer–Emmett–Teller (BET) and Barrett–Joyner–Halenda (BJH) methodson a Quanta chrome instrument (BET, 3H-2000PS4), respectively. The chemical valence states and electronic structures of the catalysts were investigated using X-ray photoelectron spectroscopy (XPS) on an ESCALAB 250Xi instrument. The water contact angle tests of the catalysts were obtained by optical contact angle measurements (Dataphysics-OCA20). The metal content in the catalysts was determined using inductively coupled plasma mass spectrometry (ICP-MS; FLEXar-NexION300X, Perkin Elmer, USA). Ultraviolet photoelectron spectroscopy (UPS) was conducted using an X-ray photoelectron spectrometer (PHI5000 VersaProbe III).

Electrochemical analyses

Electrochemical measurements of the synthesized catalysts were carried out on a Biologic VMP3 electrochemical workstation, employing a standard three-electrode configuration and a 1.0 M KOH electrolyte solution (pH = 13.5). Electrochemical assessments were performed with a prepared NF-based catalyst (1 cm × 1 cm) serving as the working electrode, a graphite plate as the counter electrode, and a standard calomel electrode (SCE) as the reference electrode. The measured potentials were transformed to the RHE scale by applying the Nernst equation: $E(\text{vs. RHE}) = E_{\text{SCE}} + 0.059 \times \text{pH} + 0.241 \text{ V}$, and were adjusted for 100% iR compensation. To evaluate the electrochemical properties of the catalysts, linear sweep voltammetry was performed with a reverse scan across the potential range of 0 to 1.4 V

(vs. SCE) at a scan rate of 0.5 mV/s. The electrochemical surface area (ECSA) was calculated based on the double-layer capacitance (C_{dl}), obtained via cyclic voltammetry (CV) analysis. The CV measurements were conducted in the non-Faradaic potential region of 0.1 to 0.2 V (vs. SCE) at incremental scan rates ranging from 2 to 12 mV/s, specifically 2, 4, 6, 8, 10, and 12 mV/s. The formula for calculating the C_{dl} was: $C_{dl} = (j_a - j_c) / (2 \times v)$, where j_a and j_c are the anode and cathode current densities, respectively, and v denotes the scan rate. The ECSA was determined using the formula: $ECSA = C_{dl} / C_s$, where the C_s value was generally between 20 and 60 $\mu\text{F cm}^{-2}$, with an average of 40 $\mu\text{F cm}^{-2}$. Electrochemical impedance spectroscopy (EIS) measurements were conducted at a potential of 0.5 V (vs. SCE) across a frequency range from 300 kHz to 10 mHz. The resulting EIS data were subsequently analyzed and fitted using ZSimDemo software. The catalyst's stability was evaluated using chronopotentiometry at current densities of 10 mA cm^{-2} and 100 mA cm^{-2} over an extended duration. Comprehensive water splitting tests were performed in a 1.0 M KOH electrolyte, with the applied potential varying from 0 to 2.5 V and a scan rate of 5 mV/s.

In situ Raman spectroscopy experiments were performed with a specialized Raman spectrometer (InVia Qontor, Renishaw), coupled with an in situ test cell (Gaoss Union C031-1), to analyze samples in a 1.0 M KOH solution. The as-synthesized catalyst was used as the working electrode, while a carbon rod acted as the counter electrode and an Ag/AgCl electrode served as the reference electrode. The laser excitation wavelength was set to 785 nm, with each spectrum recorded over an exposure time of 10 minutes. Raman spectra were collected at a constant potential ranging from 1.0 to 1.7 V (vs. RHE) to monitor the evolution of the catalyst.

In situ electrochemical impedance spectroscopy (EIS) measurements: Simultaneous electrochemical operation and characterization were conducted by holding the potential at 0.95 to 1.45 V (vs. RHE) for a duration of 10 minutes, to obtain surface chemical composition and structural information of the materials. EIS analyses were performed across a frequency spectrum from 0.01 Hz to 300 kHz at different potentials.

In-situ ATR FTIR Measurements: In-situ attenuated total reflectance Fourier transform infrared spectroscopy (ATR-FTIR) was performed using a three-electrode system, where a catalyst/glass carbon electrode served as the working electrode, an Ag/AgCl electrode as the

reference, and a Pt wire as the counter electrode. The in-situ characterization was carried out with a FT-IR spectrometer (Nicolet 6700, Thermo-Fisher Scientific), equipped with an extended-range diamond ATR accessory. Spectral data were collected at 20 S intervals, while the electrochemical conditions were controlled using a chronoamperometric method via an electrochemical workstation. The applied potential was gradually increased from 0.95 V to 1.45 V (vs. RHE).

For processing ultraviolet photoelectron spectroscopy (UPS) data: (1) Identifying the valence band maximum (VBM). Choose a region of the data close to the top of the valence band, where a distinct change in slope occurs, and perform a linear fit. Extrapolate the fitted line to the point where it intersects the baseline. The energy at this intersection corresponds to the position of the VBM. (2) Determining the work function (Φ). The work function (Φ) is obtained by subtracting the energy difference between the cut-off edge and the Fermi level ($E_{vac} - E_F$) from the incident photon energy ($h\nu$). The formula is: $j = h\nu - (E_{vac} - E_F)$. For instance, given an incident photon energy of 21.22 eV (Helium I), and an observed energy difference of 17.28 eV between the cut-off edge and the Fermi level, the work function φ can be calculated as $\varphi = 21.22 \text{ eV} - 17.28 \text{ eV} = 3.94 \text{ eV}$.

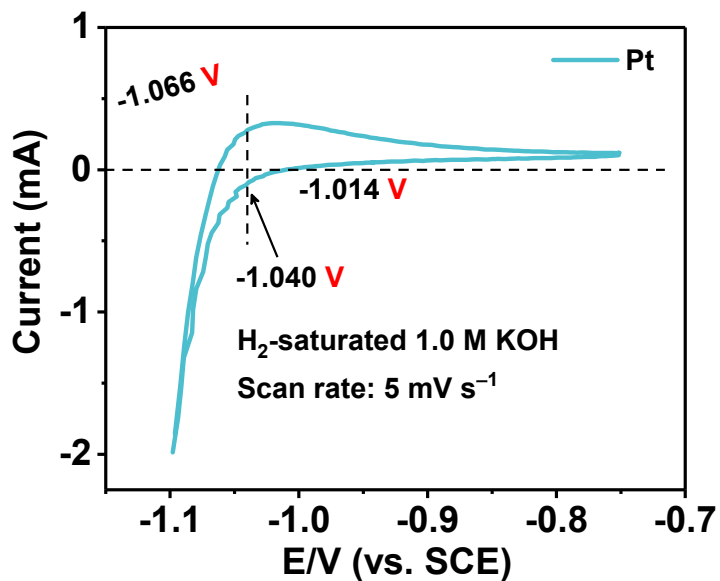


Fig. S1. RHE voltage calibration.

Calibration of the reference hydrogen electrode (RHE) was conducted in an electrolyte saturated with H₂, using a platinum wire as the working electrode. The thermodynamic potential for the hydrogen evolution reaction was obtained by averaging the two potentials at which the hydrogen electrode current is zero, with a scan rate of 5 mV/s. The results shown in the figure demonstrate that E_{SCE} was 1.040 V lower than E_{RHE} in a 1.0 M KOH solution, which matches the 1.040 V difference calculated using the Nernst equation. Given that the pH of the 1.0 M KOH solution is 13.6, the following relationship can be derived: $E_{\text{RHE}} = E_{\text{SCE}} + 0.241 \text{ V} + 0.059 \text{ V} \times \text{pH}$, which simplifies to $E_{\text{RHE}} = E_{\text{SCE}} + 1.040 \text{ V}$.

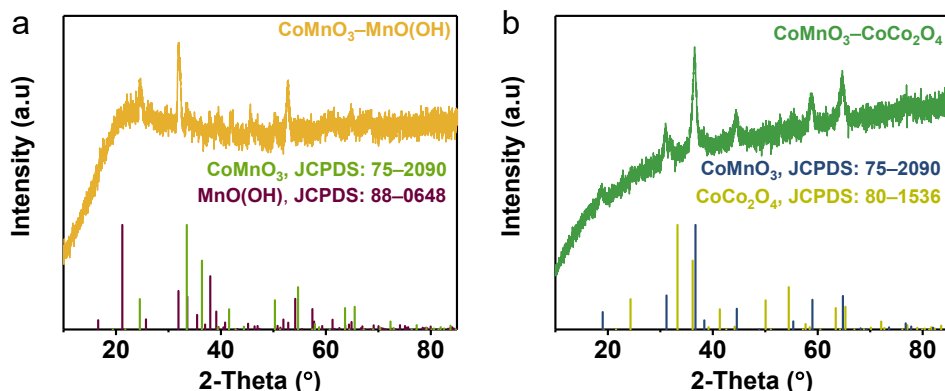


Fig. S2. XRD patterns of (a) CoMnO₃-MnO(OH)/NF and (b) CoMnO₃- CoCo₂O₄/NF.

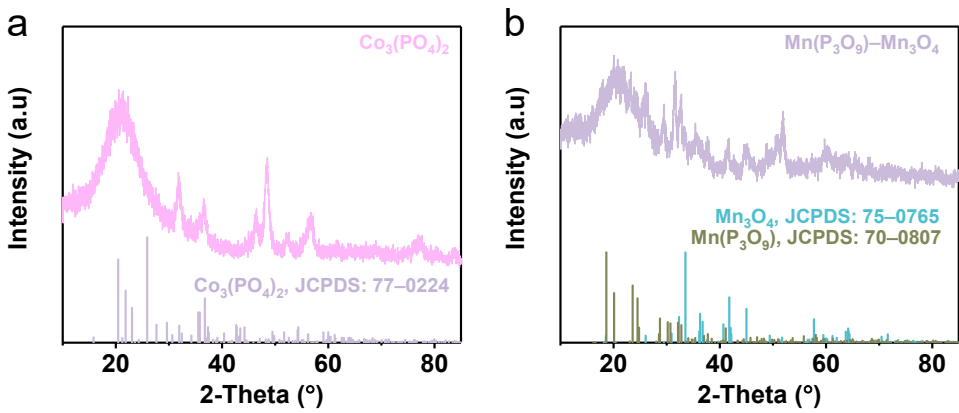


Fig. S3. XRD patterns of (a) $\text{Co}_3(\text{PO}_4)_2/\text{NF}$ and (b) $\text{Mn}(\text{P}_3\text{O}_9)-\text{Mn}_2\text{O}_3/\text{NF}$.

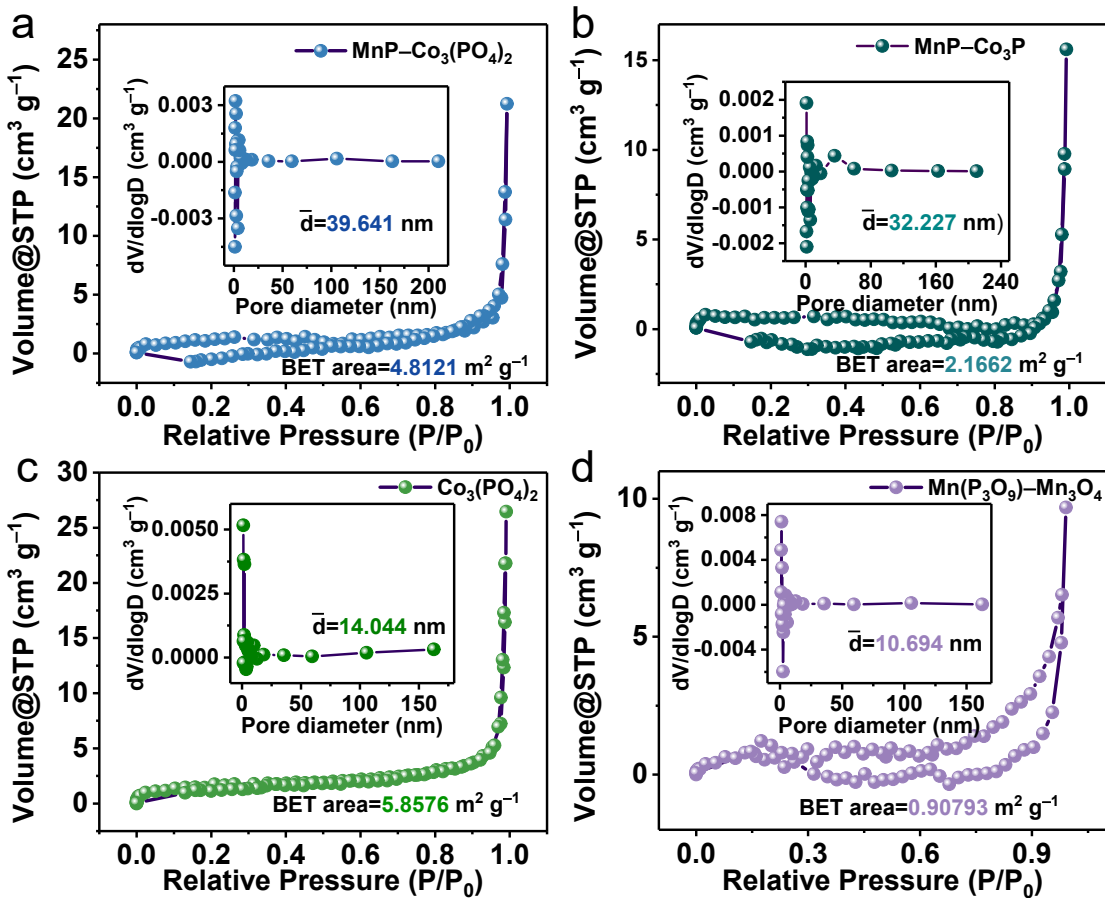


Fig. S4. N_2 adsorption/desorption isotherms and pore size distributions of (a) $\text{MnP}-\text{Co}_3(\text{PO}_4)_2/\text{NF}$, (b) $\text{MnP}-\text{Co}_3\text{P}/\text{NF}$, (c) $\text{Co}_3(\text{PO}_4)_2/\text{NF}$, and (d) $\text{Mn}(\text{P}_3\text{O}_9)-\text{Mn}_2\text{O}_3/\text{NF}$.

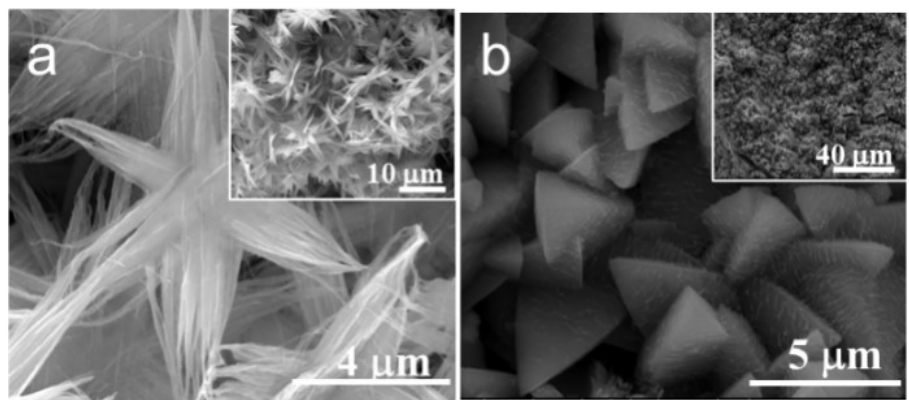


Fig. S5. SEM images of (a) $\text{Co}_3(\text{PO}_4)_2/\text{NF}$ and (b) $\text{Mn}(\text{P}_3\text{O}_9)\text{-Mn}_2\text{O}_3/\text{NF}$.

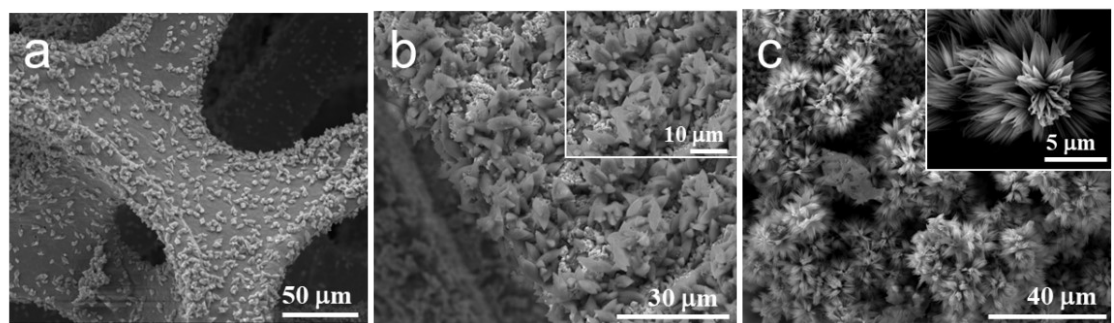


Fig. S6. SEM images of (a) $\text{CoMn}/0.5\text{--}2.5/\text{NF}$, (b) $\text{CoMn}/1.5\text{--}1.5/\text{NF}$, and (c) $\text{CoMn}/2.5\text{--}0.5/\text{NF}$.

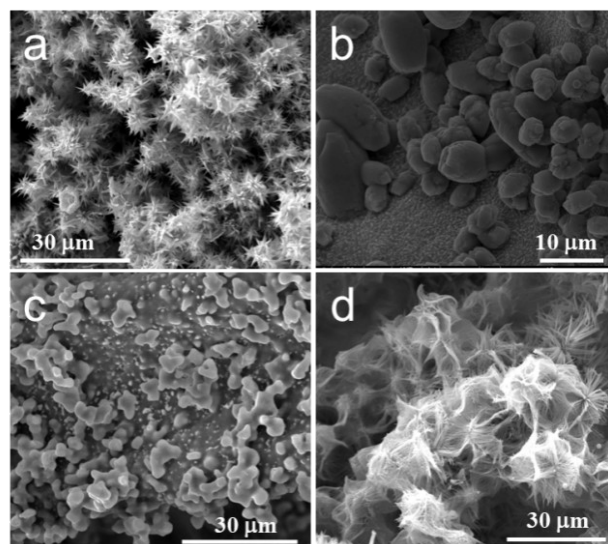


Fig. S7. SEM images of (a) $\text{CoMn}-100^\circ\text{C}/\text{NF}$, (b) $\text{CoMn}-140^\circ\text{C}/\text{NF}$, (c) $\text{CoMn}-160^\circ\text{C}/\text{NF}$, and $\text{CoMn}-180^\circ\text{C}/\text{NF}$.

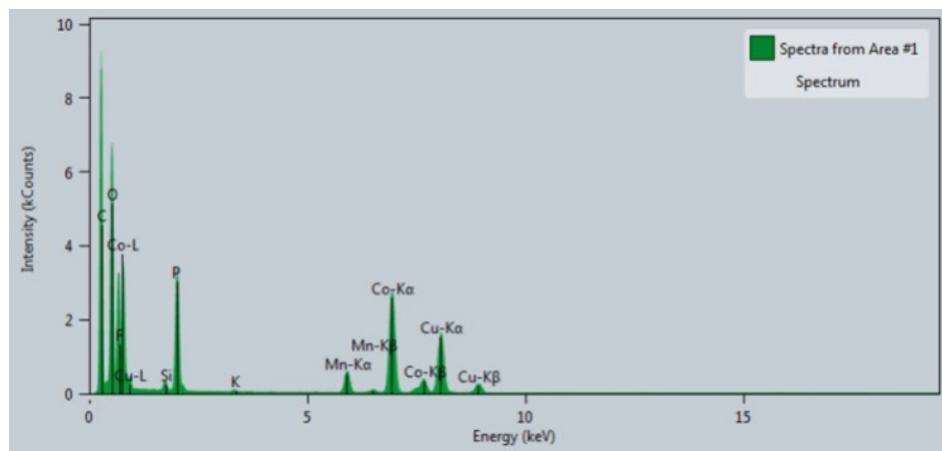


Fig. S8. EDX spectrum of $\text{MnP}-\text{Co}_3(\text{PO}_4)_2/\text{NF}$.

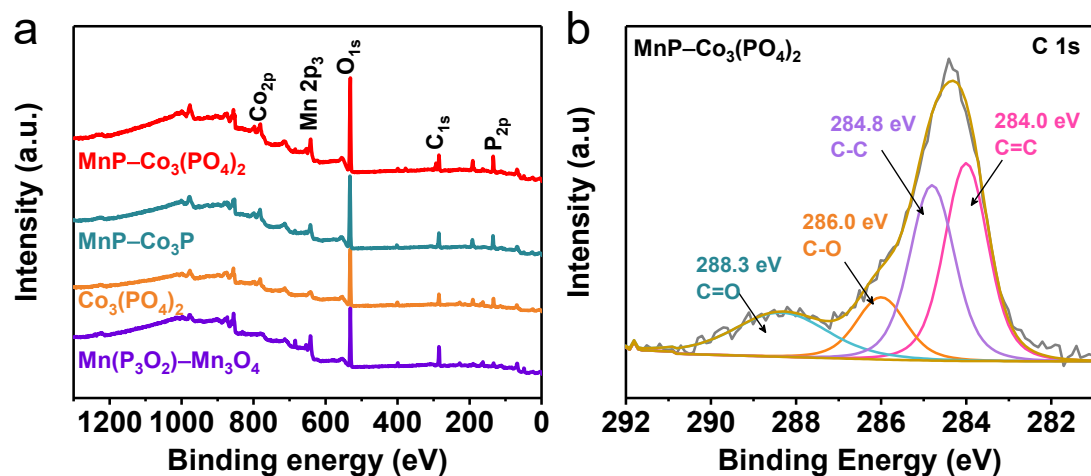


Fig. S9. (a) XPS survey spectra of $\text{MnP}-\text{Co}_3(\text{PO}_4)_2/\text{NF}$, $\text{MnP}-\text{Co}_3\text{P}/\text{NF}$, $\text{Co}_3(\text{PO}_4)_2/\text{NF}$, and $\text{Mn}(\text{P}_3\text{O}_9)-\text{Mn}_2\text{O}_3/\text{NF}$. (b) High-resolution C 1s region of $\text{MnP}-\text{Co}_3(\text{PO}_4)_2$.

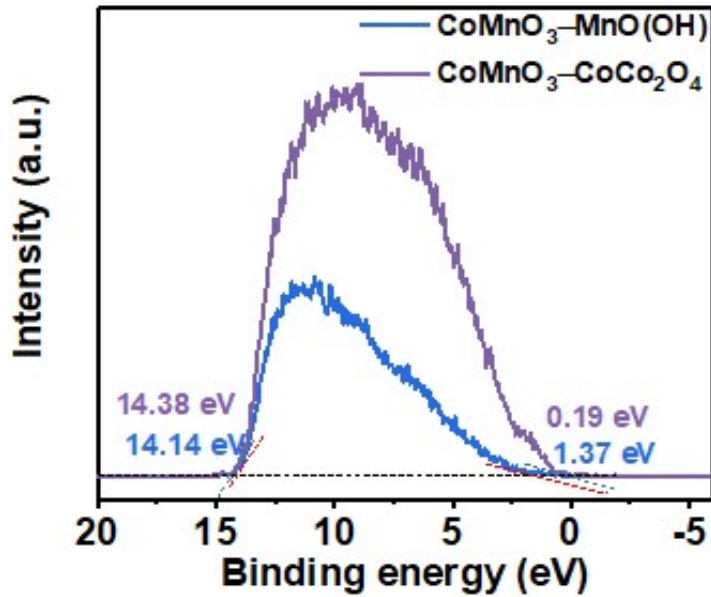


Fig. S10. Band structure alignment of $\text{CoMnO}_3\text{-MnO(OH)}/\text{NF}$ and $\text{CoMnO}_3\text{-CoCo}_2\text{O}_4/\text{NF}$.

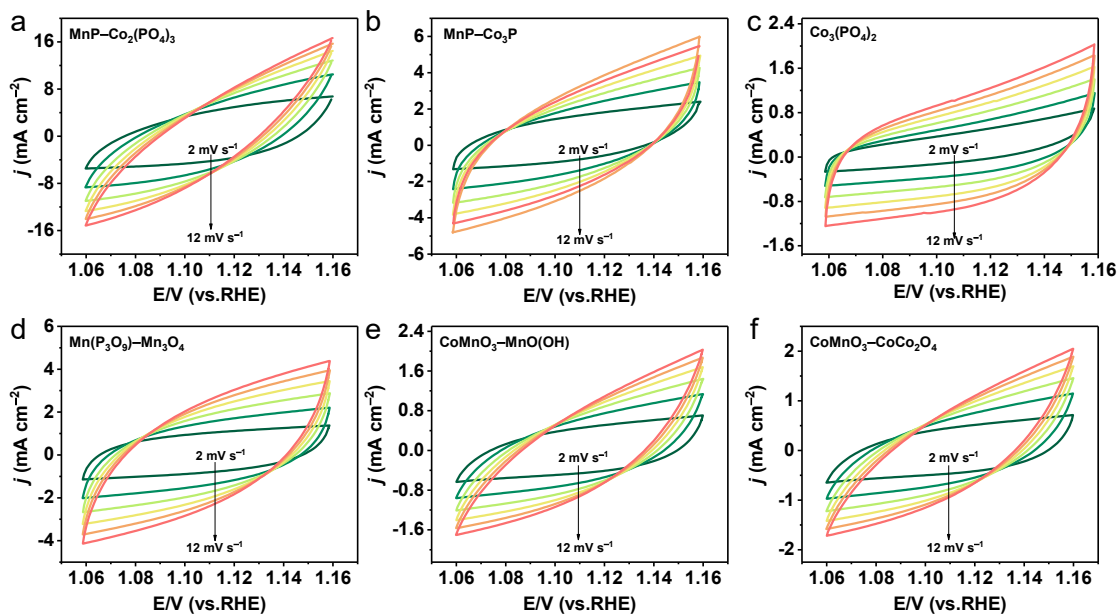


Fig. S11. Cyclic voltammograms (CVs) of (a) $\text{MnP-Co}_3(\text{PO}_4)_2/\text{NF}$, (b) $\text{MnP-Co}_3\text{P}/\text{NF}$, (c) $\text{Co}_3(\text{PO}_4)_2/\text{NF}$, (d) $\text{Mn}(\text{P}_3\text{O}_9)\text{-Mn}_3\text{O}_4/\text{NF}$, (e) $\text{CoMnO}_3\text{-MnO(OH)}/\text{NF}$ and (f) $\text{CoMnO}_3\text{-CoCo}_2\text{O}_4/\text{NF}$ at a scan rate of 2, 4, 6, 10 and 12 mV s^{-1} .

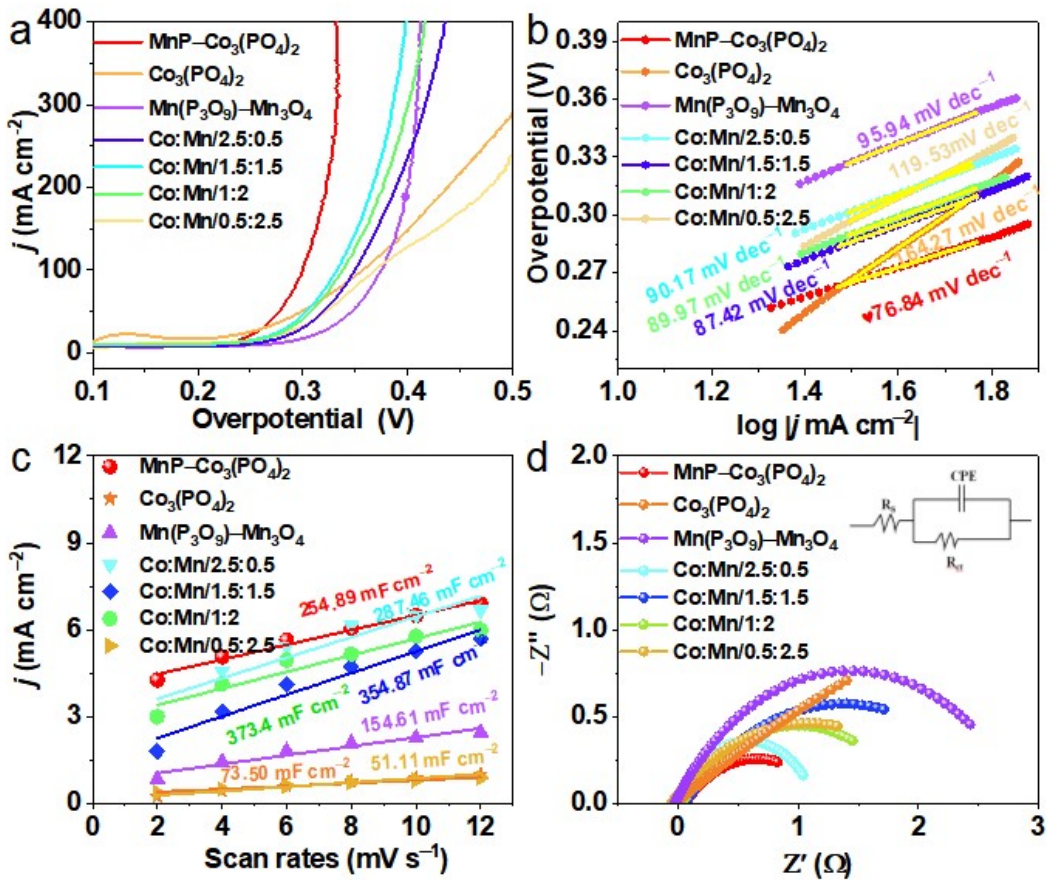


Fig. S12. OER performance of $\text{MnP}-\text{Co}_3(\text{PO}_4)_2/\text{NF}$ catalysts synthesized at different the series of samples with varying Co/Mn ratios (3/0, 0/3, 2.5/0.5, 1.5/1.5, 1/2, and 0.5/2.5). (a) Polarization curves at a scan rate of 0.5 mV s^{-1} , (b) Tafel slopes, (c) Double-layer capacitance (C_{dl}) plots, and (d) Nyquist plots of different catalysts in 1.0 M KOH solution.

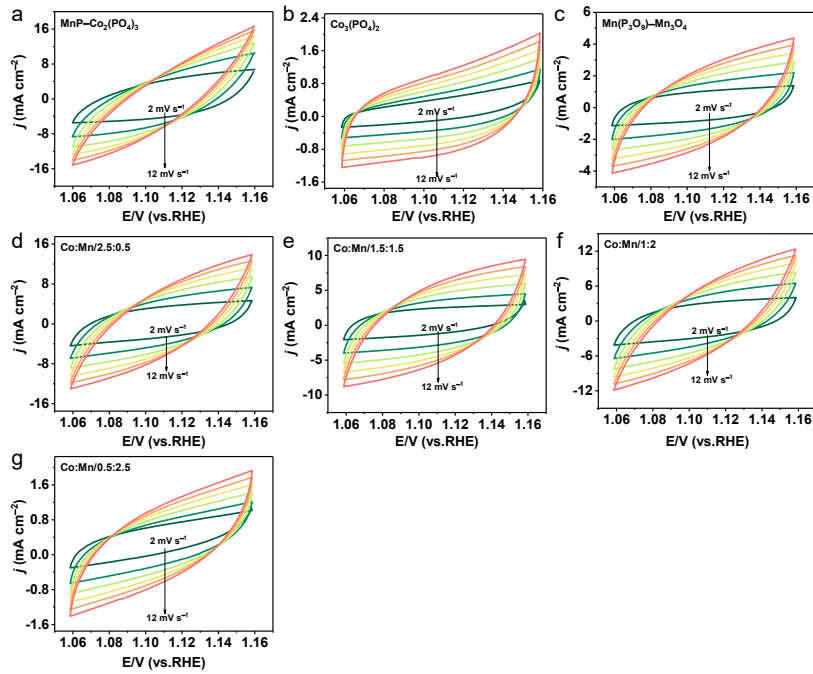


Fig. S13. Cyclic voltammograms (CVs) of $\text{MnP}-\text{Co}_3(\text{PO}_4)_2/\text{NF}$ catalysts synthesized at different the series of samples with varying Co/Mn ratios with scan rates of 2, 4, 6, 10, and 12 mV s^{-1} in 1.0 M KOH. (a) $\text{MnP}-\text{Co}_3(\text{PO}_4)_2/\text{NF}$, (b) $\text{Co}_3(\text{PO}_4)_2/\text{NF}$, (c) $\text{Mn}(\text{P}_3\text{O}_9)-\text{Mn}_2\text{O}_4/\text{NF}$, (d) $\text{CoMn}-2.5-0.5/\text{NF}$, (e) $\text{CoMn}-1.5-1.5/\text{NF}$, (f) $\text{CoMn}-1-2/\text{NF}$ and (f) $\text{CoMn}-0.5-2.5/\text{NF}$.

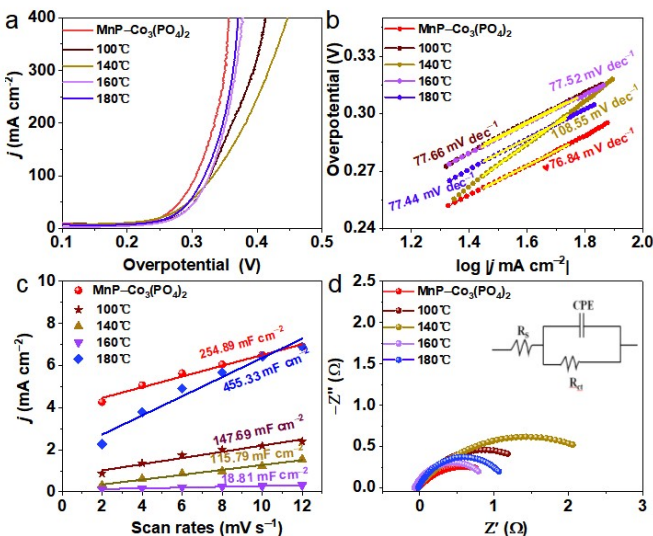


Fig. S14. OER performance of $\text{MnP}-\text{Co}_3(\text{PO}_4)_2/\text{NF}$ catalysts synthesized at different amount of temperatures for (100°C, 140°C, 160°C and 180°C). (a) Polarization curves with a scan rate of 0.5 mV s^{-1} , (b) Tafel slopes, (c) C_{dl} plots and (d) Nyquist plots of different catalysts in 1.0 M KOH solution.

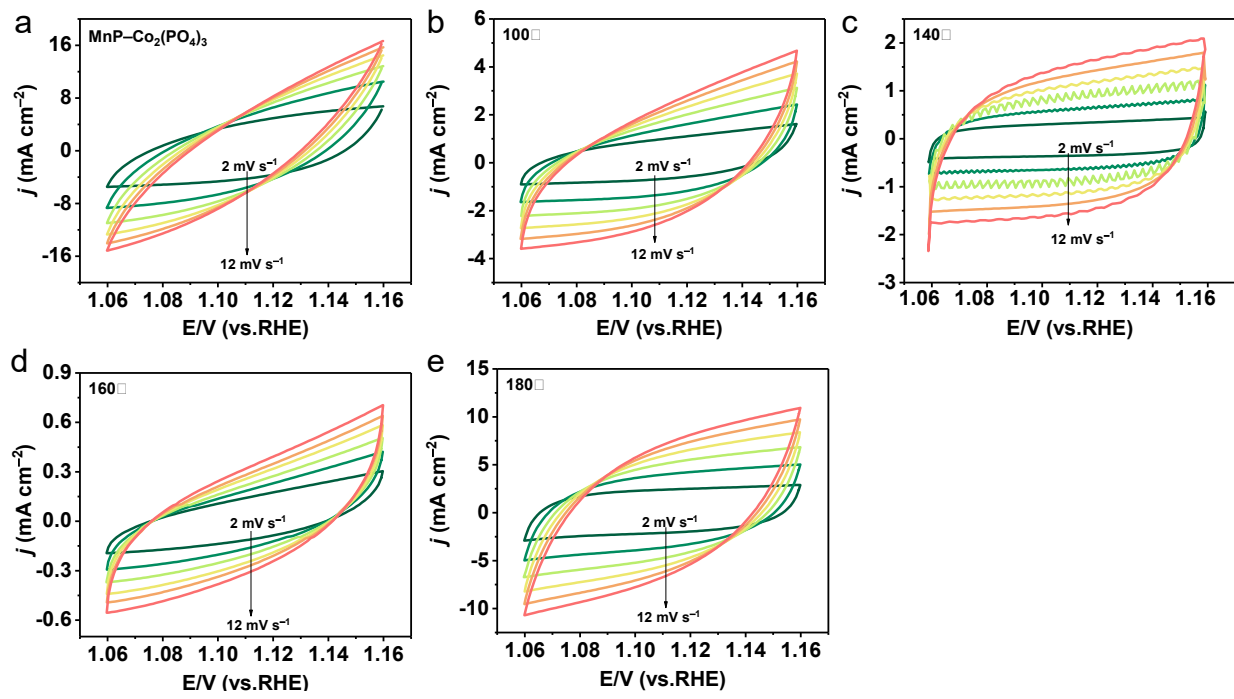


Fig. S15. Cyclic voltammograms (CVs) of MnP-Co₃(PO₄)₂/NF catalysts synthesized at different amount of temperatures at a scan rate of 2, 4, 6, 10, and 12 mV s⁻¹. (a) MnP-Co₃(PO₄)₂/NF, (b) 100°C, (c) 140°C, (d) 160°C and (e) 180°C.

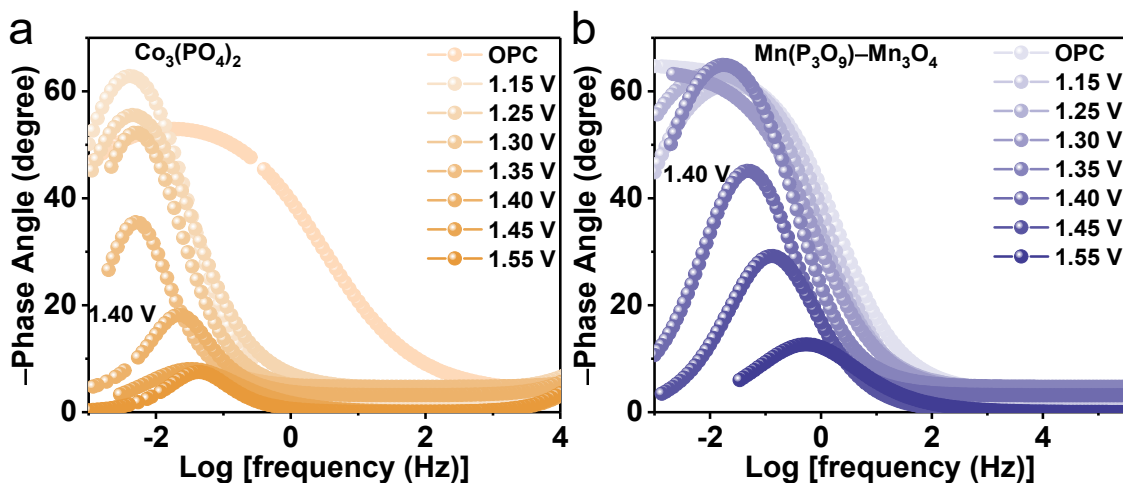


Fig. S16. EIS Bode plots of (a) Co₃(PO₄)₂/NF and (b) Mn(P₃O₉)-Mn₂O₃/NF at the potentials of 0.95-1.65 V versus RHE.

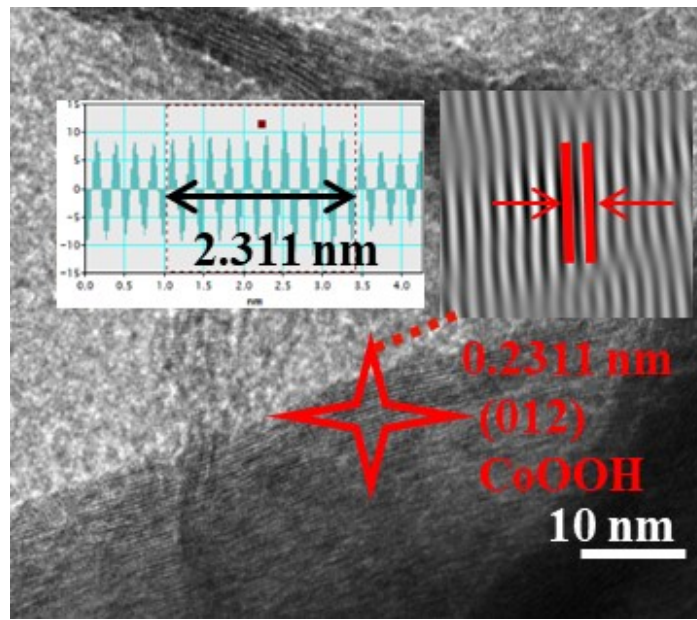


Fig. S17. HR-TEM image of MnP-Co₃(PO₄)₂/NF (the inset shows the intensity profile of corresponding areas) after long-term stability test.

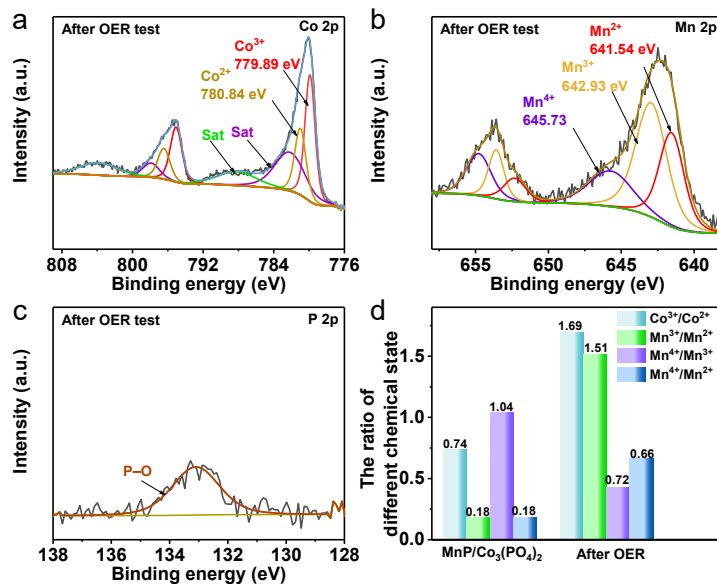


Fig. S18. (a) Co 2p, (b) Mn 2p, (c) P 2p and (d) Compare the surface molar ratios of Co³⁺/Co²⁺, Mn³⁺/Mn²⁺, Mn⁴⁺/Mn³⁺, and Mn⁴⁺/Mn²⁺ on MnP-Co₃(PO₄)₂/NF before and after long-term stability test using XPS.

Table S1. Summary of previously reported outstanding transition metal OER catalysts in alkaline solutions.

Catalyst	η_{100} (mV)	Tafel slope (mV dec ⁻¹)	Reference
MnP-Co₃(PO₄)₂	306	76.84	This work
CoMnLa _{0.2} -MOF/CF	355	95	¹
Cu-CoOOH/CFP	334	71.9	²
Co(OH) ₂ @NCNTs@NF	410	59.2	³
NiCo-H ₂ /NF	331	82.1	⁴
CoSe _{0.45} P _{1.18}	370	87	⁵
NiCoP/C	430	96	⁶
NiP ₂ /NiSe ₂	329	84	⁷
FeOOH/CoFe LDH	240	55.6	⁸
Mo-doped CoFe	331	47.8	⁹
NiCo ₂ O ₄ @Ni(Co)OOH	377	84	¹⁰
FeCo-S/Ni ₂ P/NF	279	82.1	¹¹
Ni ₂ P-VP ₂ /NF	398	49	¹²
E-Mo-NiCoP	364	76.7	¹³
Ru, Ni-CoP	360	102.3	¹⁴

Table S2. Overall water splitting performances of different catalysts in 1.0 M KOH electrolyte.

Cathodic Anodic catalysts	Electrolyte	Cell voltage (V)	Reference
MnP–Co₃(PO₄)₂	1.0 M KOH	1.58 V	This work
CoMnCH/NF	1.0 M KOH	1.68V	¹⁵
CoMn Hydroxide	1.0 M KOH	1.69V	¹⁶
Co ₂ Mn ₁ DH	1.0 M KOH	1.65V	¹⁷
CMO-H300	1.0 M KOH	1.69V	¹⁸
NiFe-LDH@Mo-NiS ₂ /NF	1.0 M KOH	1.63V	¹⁹
Co(OH) ₂ @NCNTs@NF	1.0 M KOH	1.72 V	³
Co-POC	1.0 M KOH	1.70 V	²⁰
NiCo ₂ O ₄ /NiCoP	1.0 M KOH	1.66 V	²¹
Co ₉ S ₈ -Ni ₃ S ₂ -CNTs/NF	1.0 M KOH	1.65 V	²²

References

- Y. Wang, B. Wang, X. Liu, Y. Wang, Y. Wang and Z. Liu, *ACS Appl. Energy Mater.*, 2022, **5**, 8686-8696.
- L. Yan, B. Zhang, Z. Liu and J. Zhu, *Chem. Eng. J.* , 2021, **405**, 126198.
- P. Guo, J. Wu, X.-B. Li, J. Luo, W.-M. Lau, H. Liu, X.-L. Sun and L.-M. Liu, *Nano Energy*, 2018, **47**, 96-104.
- M. Chen, D. Liu, J. Feng, P. Zhou, L. Qiao, W. Feng, Y. Chen, K. Wei Ng, S. Wang, W. Fai Ip and H. Pan, *Chem. Eng. J.* , 2022, **443**, 136432.
- Y. Zhu, H.-C. Chen, C.-S. Hsu, T.-S. Lin, C.-J. Chang, S.-C. Chang, L.-D. Tsai and H. M. Chen, *ACS Energy Lett.*, 2019, **4**, 987-994.
- P. He, X.-Y. Yu and X. W. Lou, *Angew. Chem. Int. Ed.*, 2017, **56**, 3897-3900.
- L. Yang, L. Huang, Y. Yao and L. Jiao, *Appl. Catal. B Environ. Energy*, 2021, **282**, 119584.
- D. Wang, L. Liu, Y. Liu, W. Luo, Y. Xie, T. Xiao, Y. Wang, Z. Song, H. Zhang and X.

- Wang, *ACS Sustain. Chem. Eng.* , 2023, **11**, 16479-16490.
- 9. G. Zhao, B. Wang, Q. Yan and X. Xia, *J. Alloys Compd.*, 2022, **902**, 163738.
 - 10. T. Zhou, C. Wang, Y. Shi, Y. Liang, Y. Yu and B. Zhang, *J. Mater. Chem. A*, 2020, **8**, 1631-1635.
 - 11. P. Chen, Y. Wu, X. Guo, M. Wang, C. Yu, H. Jiang, W. Zhou, G. Wu and J. Yan, *Inorg. Chem.*, 2024, **63**, 5520-5529.
 - 12. H. Yan, Y. Xie, A. Wu, Z. Cai, L. Wang, C. Tian, X. Zhang and H. Fu, *Adv. Mater.* , 2019, **31**, 1901174.
 - 13. J. Lin, Y. Yan, C. Li, X. Si, H. Wang, J. Qi, J. Cao, Z. Zhong, W. Fei and J. Feng, *Nano-Micro Lett.*, 2019, **11**, 55.
 - 14. Y. Song, J. Cheng, J. Liu, Q. Ye, X. Gao, J. Lu and Y. Cheng, *Appl. Catal. B Environ. Energy*, 2021, **298**, 120488.
 - 15. T. Tang, W.-J. Jiang, S. Niu, N. Liu, H. Luo, Y.-Y. Chen, S.-F. Jin, F. Gao, L.-J. Wan and J.-S. Hu, *J. Am. Chem. Soc.*, 2017, **139**, 8320-8328.
 - 16. J. Reddy, M. Duraivel, K. Senthil and K. Prabakar, *ChemCatChem*, 2022, **14**, e202200966.
 - 17. K. Li, D. Guo, J. Kang, B. Wei, X. Zhang and Y. Chen, *ACS Sustain. Chem. Eng.*, 2018, **6**, 14641-14651.
 - 18. Y. Pu, L. Wang, L. Jia, X. Li, W. Lu and L. Huang, *Appl. Surf. Sci.*, 2023, **636**, 157647.
 - 19. L. Wan, Z. Xu, Q. Xu, M. Pang, D. Lin, J. Liu and B. Wang, *Energy Environ. Sci.*, 2023, **16**, 1384-1430.
 - 20. H. Li, P. Wen, D. S. Itanze, M. W. Kim, S. Adhikari, C. Lu, L. Jiang, Y. Qiu and S. M. Geyer, *Adv. Mater.*, 2023, **35**, 2302628.
 - 21. W. Jin, J. Chen, H. Wu, N. Zang, Q. Li, W. Cai and Z. Wu, *Catal. Sci. Technol.*, 2020, **10**, 5559-5565.
 - 22. Y. Yao, J. He, L. Ma, J. Wang, L. Peng, X. Zhu, K. Li and M. Qu, *J. Colloid Interface Sci.* , 2022, **616**, 287-297.